Available online at www.sciencedirect.com
ScienceDirect
International Journal of Heat and Fluid Flow 29 (2008) 792–802
International Journal of HEAT AND FLUID FLOW
www.elsevier.com/locate/ijhff

Measurement of fine scale structure in turbulence by time-resolved dual-plane stereoscopic PIV

M. Tanahashi *, T. Hirayama, S. Taka, T. Miyauchi

Department of Mechanical and Aerospace Engineering, Tokyo Institute of Technology, 2-12-1 Ookayama, Meguro-ku, Tokyo 152-8850, Japan

Received 8 November 2007; received in revised form 12 February 2008; accepted 14 February 2008
Available online 18 April 2008

Abstract

To investigate fine scale structure of turbulent flows, time-resolved dual-plane stereoscopic particle image velocimetry (TRDPSPIV) has been developed using high-repetition-rate Nd:YAG lasers for industrial processing and high-speed CMOS cameras. This system provides all three velocity components and nine velocity gradients with high spatial and temporal resolution. The number of lasers used in this system is only two by adopting newly-developed parallel beam forming optics. The developed system was applied to velocity measurements of a turbulent jet with the same spatial resolution of general direct numerical simulation (DNS) of turbulence. The velocities obtained in both planes showed very similar pattern, and energy spectra in the both planes coincide very well because of the small distance between the planes. It is shown that probability density functions of the measured nine velocity gradients agree well with those obtained from DNS. From these velocity gradients, various flow properties such as vorticity vectors, second invariant of velocity gradient tensor and energy dissipation rate are obtained exactly. These properties allow an eddy identification, which has been used in the analysis of DNS, to investigate fine scale structure of turbulence. Velocity distributions around the experimentally-detected fine scale eddies have an elliptic feature, and the histograms of the diameter and maximum azimuthal velocity of the detected eddy show peaks at $D/\eta \approx 10$ and $u_{\theta,\max}/u_k \approx 0.75$. These characteristics of the fine scale eddy coincide with those obtained from DNS. Experimental evidence for the existence of the coherent fine scale eddy in turbulence is given in the present study.

PACS: 47.27.−i; 47.27.De; 47.50.Ef

Keywords: Turbulence; Laser diagnostics; Time-resolved PIV; Fine scale structure

1. Introduction

In our previous studies on fine scale structure of turbulence by direct numerical simulation (DNS) (Tanahashi et al., 1997, 2001, 2004a, 2007; Wang et al., 2007), the existence of universal fine scale structure (coherent fine scale structure), which is independent of Reynolds number and type of flow field, has been revealed. The diameter and the maximum azimuthal velocity of coherent fine scale eddies can be scaled by Kolmogorov length (η) and Kolmogorov velocity (u_k). Except for near wall turbulence (Tanahashi et al., 2004a), the most expected diameter and maximum azimuthal velocity are 8η and $1.2u_k$. It should be noted that the azimuthal velocity of intense fine scale eddies reaches $3–4u'_{rms}$. Coherent fine scale eddies have strong three-dimensional characteristics and are advecting with velocity of the order of u'_{rms} (Tanahashi et al., 1999). To investigate these fine scale structures experimentally, simultaneous measurement of three velocity components and nine velocity gradients is needed.

The coherent fine scale structure in turbulence has very important roles on the friction drag at the wall (Tanahashi et al., 2004a), turbulent heat and mass transfer (Miyauchi et al., 2002), particle dispersion in turbulence, turbulent combustion (Tanahashi et al., 2000; Nada et al., 2004), etc. because this fine scale structure possesses strong swirling motion and determines the characteristics in fine scales.

* Corresponding author. Tel./fax: +81 3 5734 3181.
E-mail address: mtanahas@mes.titech.ac.jp (M. Tanahashi).

0142-727X/$ - see front matter © 2008 Elsevier Inc. All rights reserved.
doi:10.1016/j.ijheatfluidflow.2008.02.009

Particle image velocimetry (PIV), which gives instantaneous maps of the velocity field, is a useful, firmly established, non-intrusive measurement technique. To apply this PIV measurement to various industrial purposes as well as to fundamental researches, many research groups have explored extensively over the past decade. To investigate temporal sequence of turbulent flows, high temporal resolution has been required as well as high spatial resolution. The combination of PIV and high-speed photography was conducted to track an unsteady fluid flow (Vogel and Lauterborn, 1988), whereas, the use of the light scattering in the forward direction limited the spatial resolution. To record the time evolution of the gas velocity field and the flame boundary, a cinema PIV technique was used for turbulent combustion (Upatnieks et al., 2002). Image reproduction from movie camera to CCD camera is necessary to obtain vector maps for this cinema PIV. Recently, high-speed acquisition PIV with several kHz has become possible with development of high-speed CCD and CMOS cameras, and several high-repetition-rate double-pulsed Nd:YAG or YLF lasers, which are specialized for the time-resolved PIV, have been commercially available. van Doorne et al. (2003) have developed time-resolved stereoscopic PIV (TRSPIV) up to several hundred Hz by using an Nd:YLF laser and CMOS cameras for the measurement of turbulent water flow in a pipe. To investigate turbulence characteristics in detail, however, higher spatial and temporal resolution up to several tens kHz is required. Especially, to understand the dynamics of vortical structure and its relations to turbulence statistics, sequential images of eddy motions with high temporal resolution are necessary. In our previous studies, we have developed TRSPIV up to 26.7 kHz (Tanahashi et al., 2003, 2004b) by adopting Nd:YAG lasers for industrial processing and CMOS cameras.

Measurement methods of nine velocity gradient have also been developed to obtain more detailed flow properties. Kähler and Kompenhans (2000) first proposed dual-plane stereoscopic PIV (DPSPIV) (they called it multiple plane stereo PIV). They separated the scattering light from parallel laser sheets by using orthogonally polarized light sheets with polarizing beam-splitters. Hu et al. (2001) measured large-scale structure of a lobbed jet flow with DPSPIV by the same principle. Another way to separate the scattering light was proposed by Mullin and Dahm (2005, 2006). Instead of polarization, they used green and red light sheets with color filters. However, DPSPIV is limited to instantaneous measurement of nine velocity gradients and TRSPIV is limited to time-resolved measurement of three velocity components as described above. Both of PIV techniques are not enough to measure dynamics of fine scale structure in turbulence.

More recently, tomographic PIV, which provides three velocity components in three-dimensional measurement volume, has been developed by Elsinga et al. (2006), and is capable of extending to time-resolved measurement by utilizing high-speed cameras and lasers (Scarano et al., 2007). In tomographic PIV, first, particle field in the measurement volume is reconstructed from particle images captured with several cameras. Then, three velocity components in three-dimensional volume are evaluated by means of three-dimensional cross correlation. Consequently, this technique requires the large depth of field δz, which is given as (Prasad and Jensen, 1995)

$$\delta z = 4(1 + M^{-1})^2 f_{\#}^2 \Lambda, \tag{1}$$

where M is the camera magnification, $f_{\#}$ is the f-number and Λ is the wavelength of the illumination. This requirement for the magnification and the f-number can be the limitation for the spatial resolution, and another requirement of relatively low particle density in this technique can also affect the spatial resolution.

In this study, time-resolved dual-plane stereoscopic PIV (TRDPSPIV), which provides all three velocity components and nine velocity gradients with high spatial and temporal resolutions, has been developed by using only two laser heads. Fine scale structure of turbulence was measured in a turbulent jet by the developed TRDPSPIV, and the obtained results were compared with DNS in detail.

2. Time-resolved dual-plane stereoscopic PIV

2.1. System setup

Fig. 1a shows a schematic of the time-resolved dual-plane stereoscopic PIV system. This system consists of two high-repetition-rate Nd:YAG lasers (Lee Laser, LDP-100MQG), several optics, four CMOS cameras

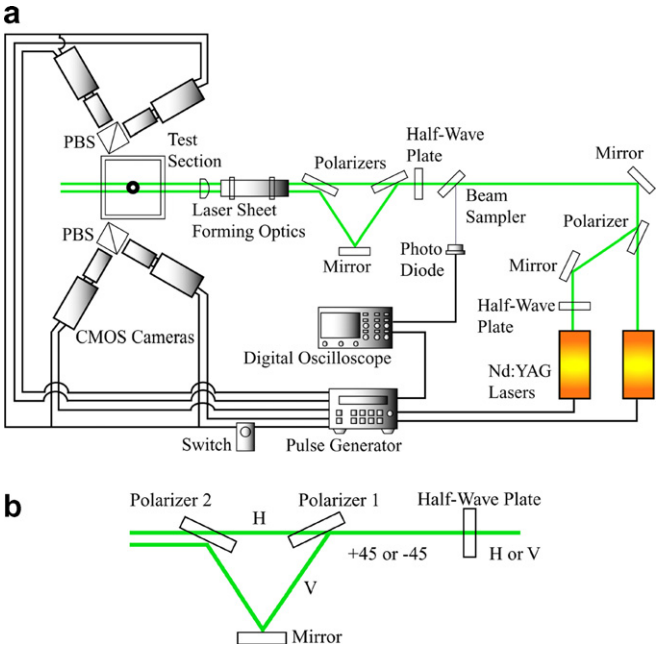

Fig. 1. Schematic of time-resolved dual-plane stereoscopic PIV system (a) and parallel beam forming optics (b).

(Vision Research, Phantom V7.1) and a pulse generator (LabSmith, LC880). The frequency of Nd:YAG lasers in conventional PIV has been no more than several tens Hz. However, in this system, we have adopted high power and high-repetition-rate pulse lasers for industrial processing as a light source. The maximum power of these lasers is 50 W at 10 kHz. To obtain required spatial resolution, each CMOS camera is equipped with a macro lens (Nikon, Micro-Nikkor 200 mm/f4) and a teleconverter (Kenko, Teleplus MC7) which doubles the focal length.

Laser beams from two lasers become doubled-pulsed beams through the laser beam combining optics which include a half-wave plate (CVI Laser) and a polarizer (CVI Laser), and each beam is divided into two parallel beams for dual-plane laser sheets through the newly-developed parallel beam forming optics shown in Fig. 1b. In Fig. 1b, H and V represent horizontal and vertical polarization, respectively. Polarization of each beam, which has horizontal or vertical polarization, rotates 45° through the half-wave plate, and each beam is divided into two beams at the first polarizer. One beam which has horizontal polarization passes through the first polarizer, and the other which has vertical polarization is reflected. Then, at the second polarizer, parallel beam is formed. The divided laser beams are expanded by sheet forming optics. After the illumination of the tracer particles with polarized laser beam, the polarizing beam splitter cube separates the incident wave-front scattered from the particles in two parts. The CMOS cameras are located with 18° inclined forward with respect to normal to the measurement plane to capture forward-scattered light. Since Scheimpflug condition is not satisfied in this camera configuration, f-number needs to be large value to focus on a broad range of the viewing area. In this study, only using two Nd:YAG lasers, DPSPIV is realized by adopting the parallel beam forming optics, which means that there is no need to add lasers to conventional PIV system for the measurement of DPSPIV. Note that most of DPSPIV systems require four lasers (Kähler and Kompenhans, 2000; Hu et al., 2001; Mullin and Dahm, 2005), except for Ganapathisubramani et al. (2005) in which a non-polarizing beam splitter is used to divide a beam.

The CMOS camera used in this study can record images with 512×256 pixels at 15.8 kHz or 256×256 pixels at 26.7 kHz. For the maximum resolution (800×600 pixels), this camera can record at 4.8 kHz. The CMOS camera starts to expose 3 μs after the trigger negative edge. Beams from each laser are synchronized to each frame interval. Repetition-rates of two Nd:YAG lasers are a half of the camera frame rate respectively and velocity vectors are calculated from successive images by a cross correlation method. Generally, cameras need the dead time (T_S) to store data between camera frames and the time interval of successive images (Δt) is limited by this dead time. The theoretical minimum T_S of the CMOS camera used in this study is about 5 μs. The images can be acquired with $\Delta t = 7$ μs in our preliminary test, which means that this PIV system can be applicable to relatively high-speed flows.

2.2. Characteristics of dual-plane laser sheets

In DPSPIV, it is important to estimate the distance between two measurement planes because the distance directly affects the results of velocity derivatives in the out-of-plane direction $\partial u_i/\partial z$. In addition, the parallelism also affects the accuracy for $\partial u_i/\partial z$, and the thicknesses determine the spatial resolution in the z direction. Mullin and Dahm (2005) measured these values by traversing a knife edge and detecting the transmitted light onto a photodiode. Ganapathisubramani et al. (2005) adopted the "burn method" to estimate them easily and roughly. In the present system, these values are measured by traversing a photodiode with a 10 μm-pinhole across the laser sheets at 3×3 points with 5 mm spacing in the traveling direction of the laser sheets and 3 mm spacing in the direction normal to it.

Fig. 2 shows one example of the measured intensity profiles of the dual-plane laser sheets for each laser with Gaussian fits. Here, z represents the coordinate normal to the laser sheets. The laser sheets for two lasers with the same polarization coincide very well and have almost the same intensity. From the Gaussian fits of these profiles, the center of the laser sheets and the half value of the intensity are determined. These locations are plotted in Fig. 3. The coordinate parallel to the light path is denoted by y. This figure also confirms the good agreement of the path of the two laser sheets. It is found that the laser-sheet thicknesses do not vary significantly through the measurement region because of the relatively long focal length (1000 mm) of cylindrical lens for generating the waist. Since the distance between two laser sheets can be set arbitrarily within about 700 μm by translating the second polarizer in the parallel beam forming optics shown in Fig. 1b, the laser sheets are aligned appropriately to prevent them from overlapping with each other.

Parallelism between the laser sheets is examined from the distribution of the center points in x and y directions.

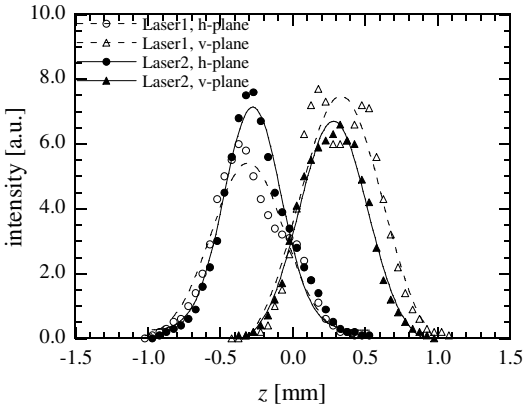

Fig. 2. Intensity profile of the dual-plane laser sheets in the perspective direction at the center of the measurement region.

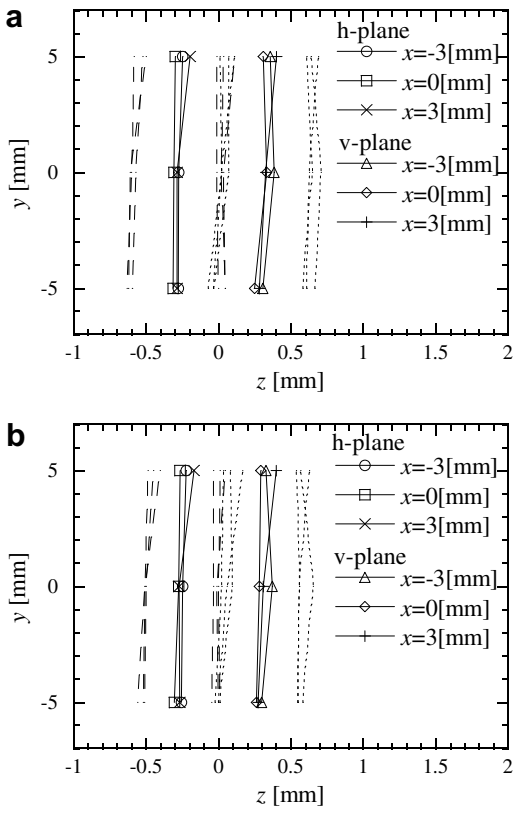

Fig. 3. Distribution of the peak and half value of the laser intensity for laser 1 (a) and laser 2 (b). Solid lines represent the peak (i.e. the center of the laser sheets), and broken lines and dotted lines do the half value.

As a result, the divergence angle between two planes is less than 3.18 mrad, which is enough for DPSPIV. To evaluate the error due to the scattering from other plane, polarized light intensities from single polarized laser beam exposure was measured. The error due to the scattering on the other plane is less than 3.5%.

2.3. Velocities and gradients

Velocity vectors are computed using 48×48 pixels interrogation window for 1st step and 24×24 pixels for second (final) step with overlap of 50% for final interrogation window. From two-dimensional velocity fields obtained by each CMOS camera, three-component velocity vectors on a two-dimensional plane are calculated by using a geometrical relation (Willert, 1997; Prasad, 2000). Although 2D or 3D calibration methods (Soloff et al., 1997; Prasad, 2000) are now available in the process of reconstruction of three-component velocity, we adopted the geometric reconstruction to decrease the computational load (the amount of measured data is 16.6 GB/s in this PIV system).

In this study, spatial cutoff filter developed by our previous study (Tanahashi et al., 2002) is used to eliminate high-wave-number noises introduced by the overlap of the interrogation windows. Note that number of the spurious vectors included in the raw data is very few (less than 0.5%) in the present measurements since the spatial resolution (size of the interrogation region) is nearly the same as that of DNS, and the elimination scheme is mainly used to cutoff the high-wave-number noises which exceed the spatial resolution of PIV. The effect of this spatial cutoff filter is discussed in Section 2.4.

As spurious vectors cannot be completely eliminated by instantaneous velocity vectors, temporal cutoff filter developed in our previous works (Tanahashi et al., 2003, 2004b), which is an advantage of the present time-resolved PIV, was also adopted at each velocity-defined point. The effectiveness of the temporal cutoff filter is shown in Section 4.

From the three velocity components on the dual planes, nine velocity gradients on the central plane between the dual planes are calculated. The velocities are linearly interpolated, and velocity gradients in the in-plane directions ($\partial u_i/\partial x$ and $\partial u_i/\partial y$) are derived by 4th-order central finite difference scheme using the interpolated velocities. Velocity gradients in the out-of-plane directions ($\partial u_i/\partial z$) are calculated by 2nd-order central finite difference scheme using the velocities on the dual planes.

2.4. Effect of spatial cutoff filter

To ensure the accuracy of the PIV measurement, the elimination scheme of the spurious vectors and noises was examined by means of a PIV simulation based on DNS of particle-laden homogeneous isotropic turbulence which was conducted by using a spectral method with $96 \times 96 \times 96$ grid points. Reynolds number based on Taylor microscale Re_λ is set to 37.1. The computational domain size is selected to be $4.5 \times 4.5 \times 4.5\ \mathrm{cm}^3$, supposing water flow with nylon 12 particles (diameter is 20 μm). The fluid velocities at particles at every time step are determined from the fluid velocity at the collocation grids by using three-dimensional cubic spline interpolation. The differential equations of particle location are integrated by 2nd-order Adams–Bashforth scheme. The calculation of homogeneous isotropic turbulence is conducted until the velocity field attains fully developed state without particles. After that, the particles are seeded randomly and the calculation with particles is started. When particles are well mixed by the turbulent motion, the results are used to construct PIV images. Laser sheet is supposed to be thickness of 1.0 mm with 1/60 s time interval. The synthetic particle images are produced at every grid points in the z direction with 1024×1024 pixels by assuming Gaussian intensity distributions for scattering light.

Fig. 4a shows velocity vectors calculated from the synthetic particle images using 32×32 pixels interrogation window with 50% overlap. Even if the particle images do not include the systematic errors due to experimental setup, the obtained velocity vectors include spurious vectors as indicated with circles in Fig. 4a, which can be seen more easily by comparing with DNS data shown in Fig. 4c. In Fig. 5, energy spectra obtained from PIV and DNS are compared. The result of PIV shows good agreement with

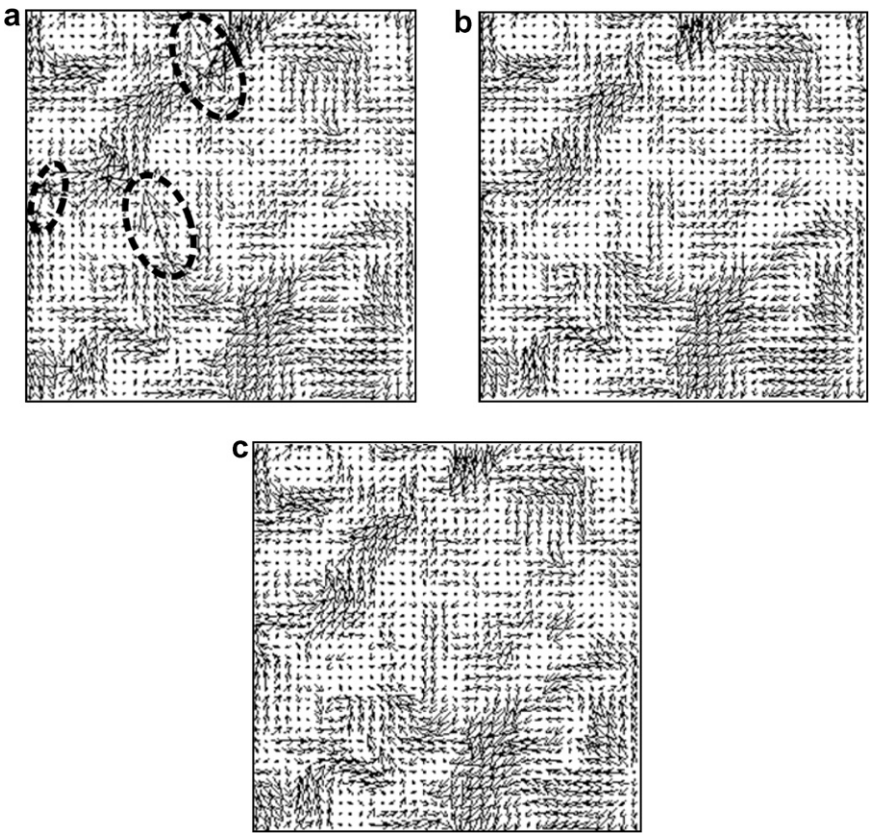

Fig. 4. Velocity vectors calculated from the simulated particle images without the spatial cutoff filter (raw data) (a), with the filter corresponding to spatial resolution of PIV (b) and those obtained from DNS (c).

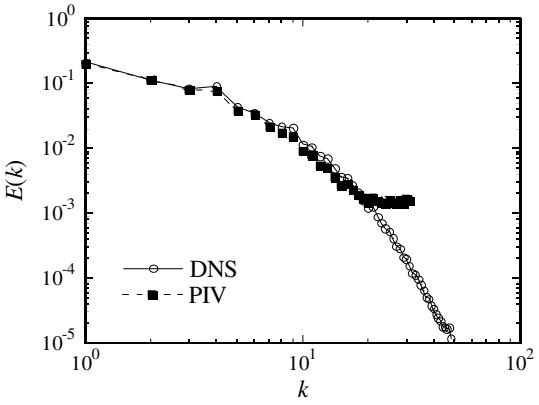

Fig. 5. Comparison of energy spectra obtained from simulated PIV and DNS.

that of DNS in the range of $k < 16$. The wave number $k = 16$ corresponds to the spatial resolution of PIV: $2k_{max}$ = total pixels/interrogation pixels (1024 pixels/32 pixels in this situation). The energy in higher wave number ($k > 16$) is generated by the overlap of the interrogation windows, and does not coincide with DNS data. Fig. 4b shows velocity vectors with the spatial cutoff filter which removes noises higher than $k = 16$. The distribution of the velocity vectors agrees with that of exact vectors obtained from DNS.

In Tables 1 and 2, correlation coefficients between the results from simulated PIV and DNS data are shown for velocities and velocity gradients. For comparison, the results from the velocity interpolated by eight surrounding points instead of those from the spatial cutoff filter are also shown in Tables 1 and 2. The modified Thompson-τ technique, which ensures that elimination of correct vectors is limited within 5%, is adopted for the elimination scheme of spurious vectors for the interpolation method. The correlation coefficients for three velocity components do not depend on the elimination technique of spurious vectors, while those for nine velocity gradients are largely affected by the elimination technique. The correlation of velocity gradients corrected with the interpolation does not show any improvement. However, with the filtering technique, velocity gradients can be estimated with high accuracy, which is 40% better than that with the interpolation technique. Therefore, the spatial cutoff filtering method is adopted in this study.

Table 1
Correlation coefficients between velocities from simulated PIV and DNS

	Raw data	Interpolation	Spatial cutoff filter
u	0.944	0.948	0.981
v	0.951	0.955	0.982
w	0.940	0.944	0.980

Table 2
Correlation coefficients between velocity gradients from simulated PIV and DNS

	Raw data	Interpolation	Spatial cutoff filter
$\partial u/\partial x$	0.403	0.408	0.793
$\partial u/\partial y$	0.533	0.539	0.826
$\partial u/\partial z$	0.397	0.412	0.825
$\partial v/\partial x$	0.534	0.540	0.820
$\partial v/\partial y$	0.432	0.438	0.803
$\partial v/\partial z$	0.419	0.436	0.824
$\partial w/\partial x$	0.506	0.511	0.814
$\partial w/\partial y$	0.519	0.524	0.820
$\partial w/\partial z$	0.281	0.293	0.792

In Table 2, the correlations of longitudinal derivatives are lower than those of the others. The reason of the low correlation coefficients of longitudinal derivatives is not clear. However, these low coefficients might be caused by the followings: fluid motion is strongly constrained by the continuity equation ($\partial u_i/\partial x_i = 0$), whereas, the motion of particles dose not obey such a restraint condition.

3. Experimental apparatus and conditions

In this study, fine scale structure of a turbulent jet is measured by TRDPSPIV. As for the near wall turbulence, fine scale eddies such as streamwise vortices and hairpin vortices have been measured by Adrian et al. (2000) and Ganapathisubramani et al. (2005). Although these eddies are kinds of coherent fine scale structure as shown by Tanahashi et al. (2004a), several problems such as reflections of laser light at wall might be encountered in capturing those eddies near the wall.

Fig. 6 shows the experimental apparatus of the turbulent jet. Air from a compressor is regulated to a constant pressure and constant flow rate by pressure regulators and a digital mass flow controller, and is seeded with droplets generated by an atomizer (TSI, Six-Jet Atomizer, Model 9306). Then, the air is led to a nozzle to form a jet. In this study, DOS (dioctyl sebacate) was used as tracer particles (mean diameter is approximately 1 μm). The orthogonal polarization of the scattered light is maintained by adopting liquid particles. The external and internal diameters of the nozzle are 12 mm and 4 mm, respectively. To prevent spreading of particles to circumference, the test section is surrounded by an acrylic duct with cross section of $32 \times 32\ \mathrm{cm}^2$.

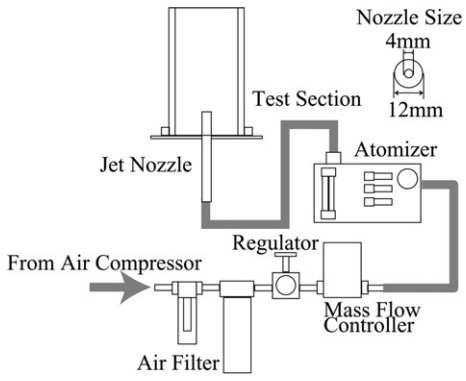

Fig. 6. Experimental apparatus of a turbulent jet.

In this study, measurement was carried out at $Re_d = 5316$, $x/d = 60$ and $r/d = 0$, where Re_d is Reynolds number based on the nozzle diameter d and mean axial velocity at the jet exit. x is distance from the jet exit and r denotes the radial coordinate. Preliminary measurements by a hot-wire constant temperature anemometer with x-probe (Kanomax Japan, Model0250R, tungsten, ∅5 μm) show that mean velocity $u_m = 1.63$ m/s, rms of velocity fluctuation $u'_{rms} = 0.443$ m/s, Taylor microscale $\lambda = 2.13$ mm, Kolmogorov length $\eta = 137$ μm, Kolmogorov velocity $u_k = 0.110$ m/s, and $Re_\lambda = 76.8$. The global features of the flow including u_m, u'_{rms}, rms of axial velocity fluctuation v'_{rms} and Reynolds stress $\overline{u'v'}$ were presented in our previous work (Tanahashi, 2004b), and agreed with those obtained by Wygnanski and Fiedler (1969) and Panchapakesan and Lumley (1993). Based on these statistics, the camera resolution was determined to be 512×256 pixels for $8.0 \times 4.0\ \mathrm{mm}^2$ region, which means that the spatial resolution of PIV is 2.7η (375 μm) for 24×24 pixels interrogation region. This spatial resolution is the same order of that of DNS of turbulent flows. Note that the velocity vectors are evaluated with 50% overlap. In this sense, velocity vectors are obtained every 1.35η. Frequency of four cameras is set to 15.8 kHz and repetition-rate of two Nd:YAG lasers is set to 7.9 kHz, which results in 7.9 kHz temporal resolution for the velocity measurement. Time interval between successive images (Δt) is set to 42 μs. The FWHM (full width at half maximum) of laser sheet thickness is 618 μm and 507 μm for each lasers. The thickness of the laser sheet is measured by the photodiode scanning with a 10 μm-pinhole as described in Section 2.2. The separation between two laser sheets is set to be 584 μm (4.3η). The PIV measurement was conducted during approximately 7.5 s in total.

The other relevant experimental conditions are listed in Table 3. The Stokes number based on Kolmogorov time scale $St_\eta \equiv \tau_p/\tau_\eta$ is used to evaluate the particle response to fluid motion, where τ_η is Kolmogorov time scale, and particle time scale is calculated from $\tau_p = (\rho_p/\rho_f)(d_p^2/18\nu)$ using particle density ρ_p, fluid density ρ_f and particle diameter d_p.

4. Performance of TRDPSPIV

Fig. 7 shows typical distributions of fluctuating velocity vectors and vorticity (ω_z) on the both planes with time interval 506 μs. Here, white represents positive vorticity and black does negative one. The visualized distance between two measured planes is ten times the real scale for easy understanding. Note that, since the temporal resolution of the present measurement is 7.9 kHz, time interval of each time step is 127 μs. However, to show dynamical

Table 3
Relevant experimental conditions

Seeding	Particle	Dioctyl sebacate
	Specific weight	0.91 g/cm^3
	Diameter	1 μm
	St_η	1.6×10^{-3}
Light sheet	Laser type	Nd:YAG
	Wave length	532 nm
	Energy per pulse	5 mJ/pulse
	Pulse duration	100–200 ns
Camera	Type	CMOS
	Pixel size	22 μm
	Bit depth	12bit
	Lens focal length	400 mm
Imaging	f-number	11
	Magnification	1.4
	Signal level	450/4096
	Maximum particle displacement	8 pixels

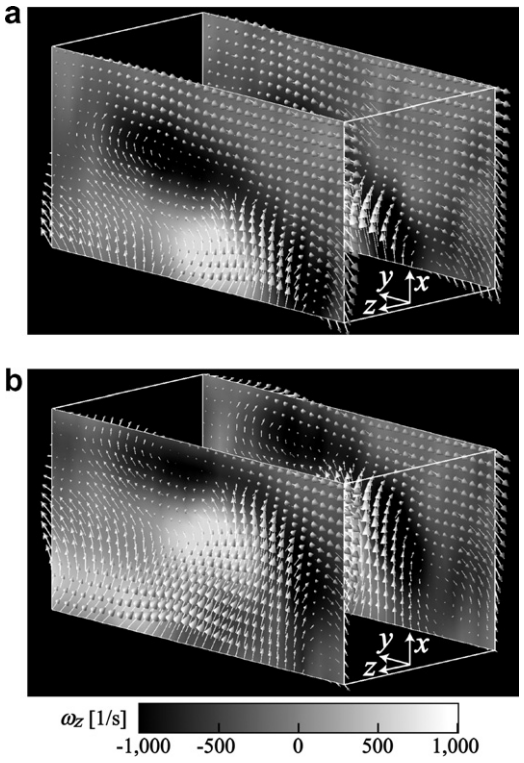

Fig. 7. Typical velocity vectors and vorticity (ω_z) distributions. Time interval between (a) and (b) is 506 μs.

behavior of vortical structure clearly, three time steps between Fig. 7a and b are skipped. Since the measurement is conducted in fully developed turbulent jet, fluctuations of velocities and vorticity are relatively high. As the distance between two planes is 4.3η, velocity and vorticity patterns are very similar in the both planes. The enough temporal resolution of the present PIV provides movies of fine scale motion in turbulence (not shown here).

Our previous study (Tanahashi, 2004b) showed that the time-resolved single-plane PIV, which is the base of the present study, can measure turbulent fluctuation which

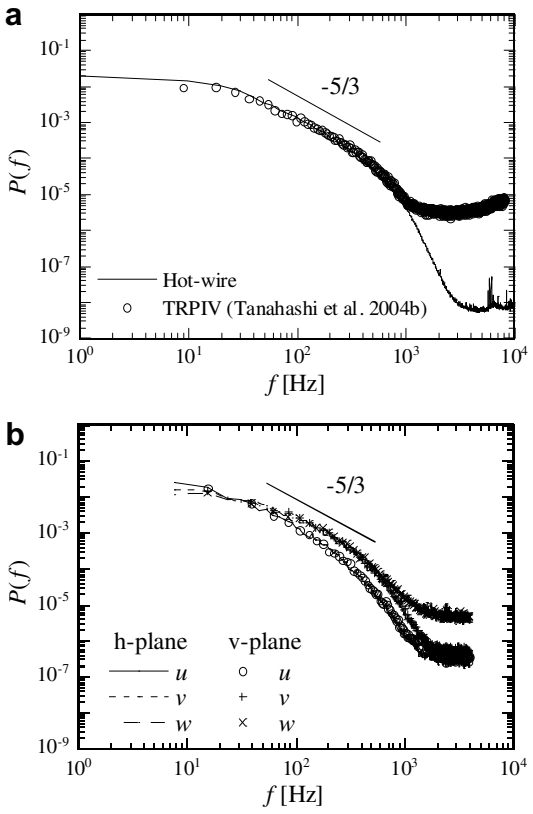

Fig. 8. Power spectra of streamwise velocity component obtained in our previous measurement (a), and those of three velocity components at the center of each polarization plane (b).

has an inertial subrange in power spectrum. In Fig. 8a, power spectra obtained from PIV and hot-wire are compared. Both spectra agree with each other except for high frequency region. In this study, power spectra of three velocity components on dual-planes can be obtained simultaneously. Fig. 8b shows power spectra measured at the center of the measurement region. The power spectra of the same velocity component coincide very well. This means that the fluctuations of velocities for the both planes coincide with each other. Although the accuracy of the out-of-plane velocity component (w) is a little bit lower than that of other velocity components in high frequency range, it is enough in the inertial subrange.

The noises observed in high frequency range of the power spectra are removed with temporal cutoff filter as mentioned in Section 2.3. Fig. 9 shows comparison of measured time series data for streamwise velocity component with and without the temporal cutoff filter. The same velocity data set is shown with both relatively wide (0–0.1 s) and narrow (0.010–0.015 s) range of time period to clearly show the effect of the temporal cutoff filter. Note that velocities at each time were already corrected by using spatial information as described in Section 2.4. The cutoff frequency is determined to be 1600 Hz from Fig. 8. Fig. 9a and b indicate that only the high frequency noises which exceed inertial subrange are removed. This mixed correction technique based on both of spatial and temporal information is

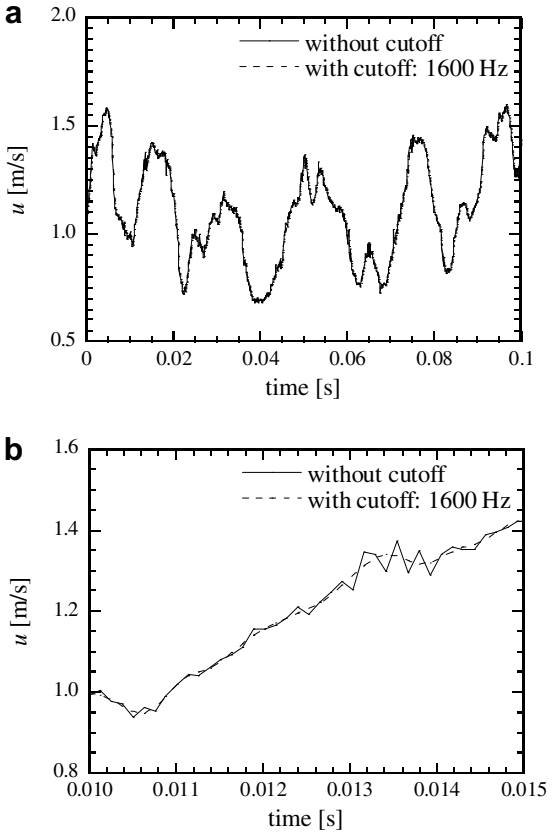

Fig. 9. Comparison of time series data for streamwise velocity component in horizontal polarization plane with and without the temporal cutoff filter. The same velocities are shown with relatively wide (a) and narrow (b) range of time period.

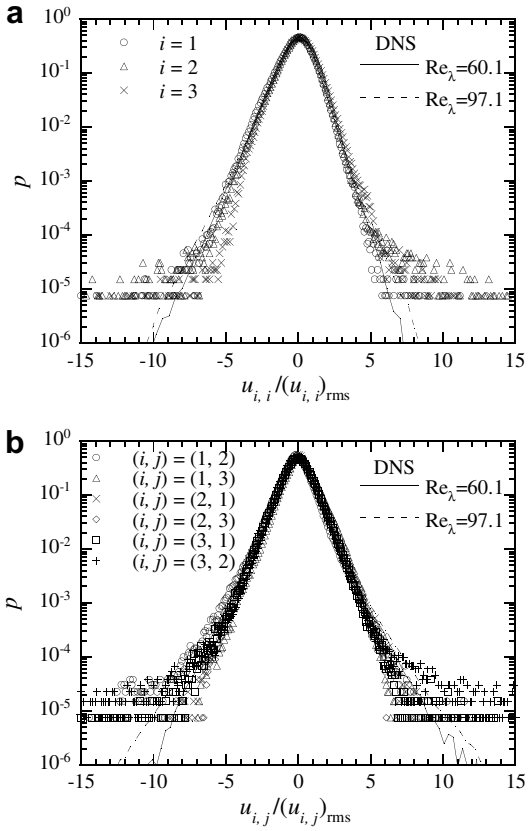

Fig. 10. Probability density functions of longitudinal (a) and lateral (b) velocity derivatives.

very effective to obtain correct velocity fluctuation of turbulence.

Probability density functions of longitudinal and lateral velocity derivatives are shown in Fig. 10a and b. The derivatives are normalized by their rms values. The results obtained from TRDPSPIV are compared with those from DNS of homogeneous isotropic turbulence with $Re_\lambda = 60.1$ and 97.1. The longitudinal and lateral velocity derivatives by TRDPSPIV agree very well with those by DNS. The shape of probability density function, which is represented by skewness and flatness factors in general, is nearly the same with that obtained by DNS. These results show that TRDPSPIV gives all velocity gradients with enough accuracy.

The accuracy of all nine velocity gradients obtained from DPSPIV was assessed carefully by Mullin and Dahm (2006). They performed "single-plane imaging assessment", "coincident-plane imaging assessment" and "separated-plane imaging assessment" to ensure the accuracy of velocity gradients. In the separated-plane imaging assessment, the divergence error $\partial u_i/\partial x_i$ for incompressible fluid was reported to estimate the accuracy of on-diagonal component of the velocity gradient tensor, and their rms value was 0.35. In this study, the divergence error is indicated for comparison in Fig. 11. Fig. 11 shows a probability density function of velocity divergence in the center of the measurement region normalized by the local norm of the velocity gradient tensor. The rms value is 0.29 for the data in the center of the measurement region and 0.33 for all the data. These results suggest that the velocity gradients are more accurate near the center, which is due to the camera configuration without Scheimpflug adapter as mentioned in Section 2.1. Nevertheless, the accuracy is enough in the entire measurement region.

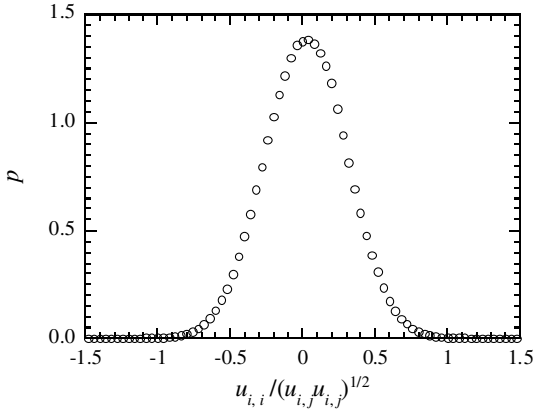

Fig. 11. Probability density function of velocity divergence $\partial u_i/\partial x_i$ normalized by the local velocity gradient norm $(\partial u_i/\partial x_j \partial u_i/\partial x_j)^{1/2}$.

From the nine-component velocity gradients obtained by the present PIV, vorticity vectors ω_i ($= \epsilon_{ijk} W_{jk}$), second invariant of velocity gradient tensor defined as

$$Q = -\frac{1}{2}(S_{ij}S_{ij} - W_{ij}W_{ij}) \tag{2}$$

and energy dissipation rate $\varepsilon (= 2\nu S_{ij}S_{ij})$ can be estimated directly without the assumptions of isotropy and Taylor's hypothesis.

Here ϵ_{ijk} is Eddington's epsilon, and S_{ij} and W_{ij} denote symmetric and antisymmetric parts of the velocity gradient tensor A_{ij};

$$A_{ij} = S_{ij} + W_{ij}, \tag{3}$$

$$S_{ij} = \frac{1}{2}\left(\frac{\partial u_i}{\partial x_j} + \frac{\partial u_j}{\partial x_i}\right), \tag{4}$$

$$W_{ij} = \frac{1}{2}\left(\frac{\partial u_i}{\partial x_j} - \frac{\partial u_j}{\partial x_i}\right). \tag{5}$$

In the present study, ω_i and Q are used for identification of fine scale eddies in turbulence, which is discussed in the next section. η and u_k obtained from the preliminary measurements by a hot-wire are estimated based on the assumption of isotropy and Taylor's hypothesis. On the other hand, since ε ($\bar{\varepsilon} = 4.85\ \mathrm{m^2/s^3}$) is derived without any assumption from the present PIV, η ($= (\nu^3/\varepsilon)^{1/4}$) and u_k ($= (\varepsilon\nu)^{1/4}$) are calculated more precisely. The results obtained by the PIV are $\eta = 162\ \mu\mathrm{m}$ and $u_k = 9.23 \times 10^{-2}\ \mathrm{m/s}$. Note that these values are calculated using the data near the center of the measurement region.

5. Characteristics of fine scale eddies

To investigate scaling law of the coherent fine scale eddies, it is necessary to identify a method for extracting vortices from instantaneous turbulent flow field. The high vorticity or enstrophy regions have been widely used to identify coherent structures and vortical structures (Hussain and Hayakawa, 1987; She et al., 1990; Jiménez and Wray, 1998). However, vorticity magnitude is not always appropriate method for identification of vortical structures, since high vorticity regions represent tube-like and sheet-like structures and they exist simultaneously in the flows with a background shear.

In our DNS studies (Tanahashi et al., 1997, 2001, 2004a; Wang et al., 2007), coherent fine scale eddies were educed without any threshold by using an identification scheme based on the local flow pattern. The identification scheme consists of the following steps (see Fig. 12):

(1) Evaluation of Q at each collocation point from the results of DNS.
(2) Probability of existence of positive maxima of Q near the collocation points is evaluated at each collocation point from the Q distribution. The case that a maximum of Q coincides with a collocation point is very rare, so it is necessary to define probability on collocation points.

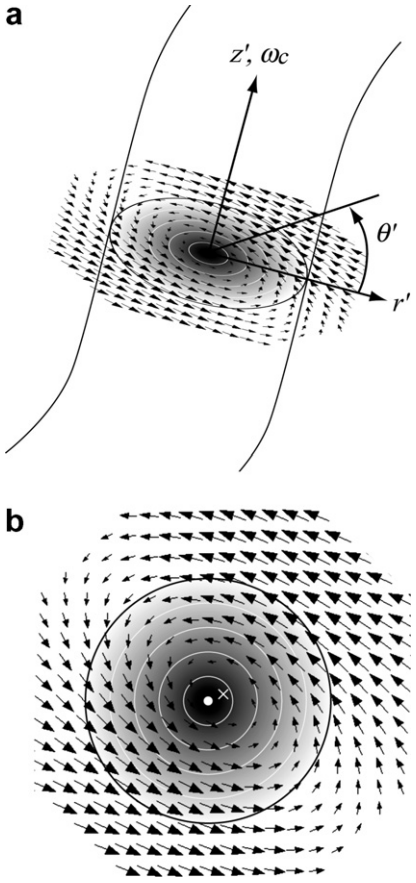

Fig. 12. Schematic of the eddy identification process. (a): a bird's-eye view of an eddy and (b): a cross section perpendicular to the eddy. Gray scale color and white contour lines show the distribution of Q around the local maximum determined in the step (3). z' is the z-axis of the cylindrical coordinate system considered in the step (4). The white closed circle denotes the local maximum of Q, and "×" does the center of the eddy determined in the step (5).

(3) Collocation points with high possibility of existence are selected to survey actual maxima of Q. Locations of Q maxima are determined by applying a three-dimensional fourth-order Lagrange interpolation to DNS data.
(4) At the maximum point of second invariant, a horizontal plane perpendicular to the vorticity vector (ω_c) is defined and a cylindrical coordinate system (r', θ', z') with the maximum point as the origin is considered. The velocity vectors are projected on this coordinate and mean azimuthal velocity is calculated.
(5) A point that has minimum variance of azimuthal velocity is surveyed near the maximum point. In this process, cylindrical coordinate system is always renewed around a new searched point.
(6) Statistical properties are calculated around the points.

From the distribution of Q, two-dimensional cross sections of the coherent fine scale eddies are identified by using this identification scheme. The educed section includes a local maximum of Q along the axis of a coherent fine scale

eddy and a center point of swirling motion is identified. As for the present study, since measured velocities are limited to dual-planes with small distance, another condition is added to the identification scheme. Eddies nearly perpendicular to the measurement planes are identified. As the spatial distribution of rotating axis of the fine scale eddy is random for fully developed turbulent flow except for near wall turbulence (Tanahashi et al., 2001, 2004a), this additional condition does not affect the results statistically.

Fig. 13a shows distribution of second invariant and velocity vectors around a typical fine scale eddy. The velocity at the center of the eddy is subtracted from the velocity field, and the color represents the second invariant. Here, white represents positive Q and black does negative one. The angle between the vorticity vector at the center of the eddy and the measurement planes is 87.3°. The asymmetric characteristic of the fine scale eddy shown in Fig. 13a agrees well with that obtained from DNS (Miyauchi et al., 2002; Kang et al., 2006). Fig. 13b shows mean azimuthal velocity profile of the typical fine scale eddy. The radius and the mean azimuthal velocity in Fig. 13b are normalized by η and u_k which are obtained from the present PIV. The radius of the fine scale eddy is defined as the distance between the center and the locations where the mean azimuthal velocity shows the maximum or minimum value. Thus, the diameter (D) of this eddy is 11.4η and the maximum azimuthal velocity ($u_{\theta,\max}$) is $2.5u_k$. Fig. 14 shows the histograms of the diameter and maximum azimuthal velocity of the fine scale eddies. The diameter and maximum azimuthal velocity are normalized by η and u_k calculated from the PIV data. Because of the limitation of the relatively small measurement region, diameter for an identifying eddy is set to less than 16η, and eddies larger than 16η are not counted in these histograms. The number of educed fine scale eddies from the above identification scheme was 74 on condition that the angles between eddies and the measurement planes are 80–90°. The histograms of the diameter and maximum azimuthal velocity show peaks at $D/\eta \approx 10$ and $u_{\theta,\max}/u_k \approx 0.75$. It should be noted that the actual peak of D might be lower than the present results because the somewhat tilted cross section of the eddies are detected in this study. In our DNS studies (Tanahashi et al., 1997, 2001, 2004a, 2007; Wang et al., 2007), it is shown that the most expected diameter and maximum azimuthal velocity are 8η and $1.2u_k$. The characteristics of the fine scale eddies obtained in the present study are very similar to those of coherent fine scale eddy which has been shown by detailed analyses of DNS. These results give experimental support for the existence of the coherent fine scale eddy in turbulence. However, since the number of educed eddies, which is 74, is insufficient in quantity, statistically-meaningful data is needed to ensure this suggestion in the future work.

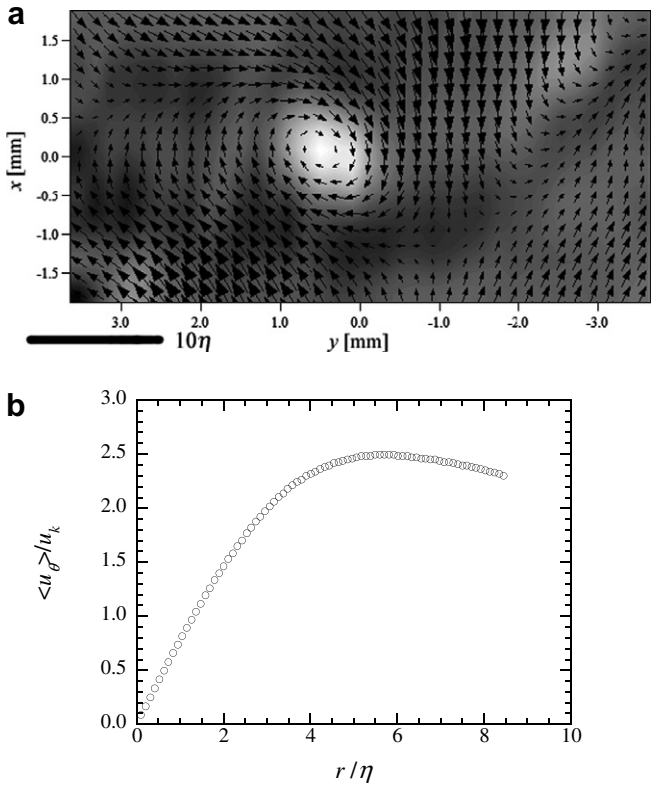

Fig. 13. Distribution of second invariant and velocity vectors around the typical fine scale eddy (a) and mean azimuthal velocity profile of the typical fine scale eddy (b).

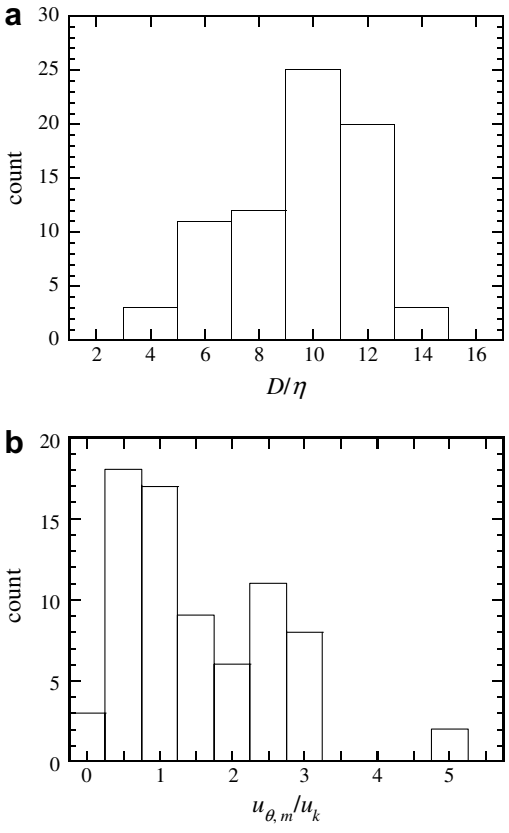

Fig. 14. Histograms of diameter (a) and maximum azimuthal velocity (b) of the measured fine scale eddies.

6. Conclusions

In this study, time-resolved dual-plane stereoscopic PIV has been developed to investigate fine scale structure of turbulence. The newly-developed parallel beam forming optics allows dual-plane stereoscopic PIV by only two lasers. The developed PIV system provides velocity vector maps on the dual-planes with high temporal resolution up to 26.7 kHz. Three velocity components and nine velocity gradients are measured with nearly the same accuracy as DNS by the time-resolved dual-plane stereoscopic PIV.

Fine scale structure of turbulence was measured in a turbulent jet with the same spatial resolution as that of DNS. Coherent fine scale eddies can be identified by the time-resolved dual-plane stereoscopic PIV using the identification scheme developed in our DNS studies. The detected fine scale eddies have asymmetric characteristics, and the histograms of the diameter and maximum azimuthal velocity show peaks at $D/\eta \approx 10$ and $u_{\theta,\max}/u_k \approx 0.75$. These characteristics are very similar to those obtained from detailed analyses of DNS, which gives experimental support for the existence of the coherent fine scale eddy in turbulence.

Acknowledgements

This work is partially supported by Grant-in-Aid for Scientific Research (S) (No. 18106004) and (B) (No. 19360097) of Japan Society for the Promotion of Science and by Grant-in-Aid for the Young Scientists (A) (No. 16686011) of the Ministry of Education, Culture, Sports, Science and Technology, Japan.

References

Adrian, R.J., Meinhart, C.D., Tomkins, C.D., 2000. Vortex organization in the outer region of the turbulent boundary layer. J. Fluid Mech. 422, 1–54.

Elsinga, G.E., Scarano, F., Wieneke, B., van Oudheusden, B.W., 2006. Tomographic particle image velocimetry. Exp. Fluids 41, 933–947.

Ganapathisubramani, B., Longmire, E.K., Marusic, I., Pothos, S., 2005. Dual-plane PIV technique to determine the complete velocity gradient tensor in a turbulent boundary layer. Exp. Fluids 39, 222–231.

Hu, H., Saga, T., Kobayashi, T., Taniguchi, N., Yasuki, M., 2001. Dual-plane stereoscopic particle image velocimetry: system set-up and its application on a lobed jet mixing flow. Exp. Fluids 31, 277–293.

Hussain, A.K.M.F., Hayakawa, M., 1987. Eduction of large-scale organized structure in a turbulent plane wake. J. Fluid Mech. 180, 193–229.

Jiménez, J., Wray, A.A., 1998. On the characteristics of vortex filaments in isotropic turbulence. J. Fluid Mech. 373, 255–285.

Kähler, C.J., Kompenhans, J., 2000. Fundamentals of multiple plane stereo particle image velocimetry. Exp. Fluids 29, 70–77.

Kang, S.-J., Tanahashi, M., Miyauchi, T., 2006. Elliptic feature of coherent fine scale eddies in turbulent channel flows. J. Mech. Sci. Technol. 20, 262–270.

Miyauchi, T., Tanahashi, M., Tanaka, N., Iwase, S., 2002. Scalar dissipation rate and coherent fine scale eddies in turbulence. In: Proceedings of International Symposium on Dynamics and Statistics of Coherent Structure in Turbulence, pp. 249–258.

Mullin, J.A., Dahm, W.J.A., 2005. Dual-plane stereo particle image velocimetry (DSPIV) for measuring velocity gradient fields at intermediate and small scales of turbulent flows. Exp. Fluids 38, 185–196.

Mullin, J.A., Dahm, W.J.A., 2006. Dual-plane stereo particle image velocimetry measurements of velocity gradient tensor fields in turbulent shear flow. I. Accuracy assessments. Phys. Fluids 18, 035101.

Nada, Y., Tanahashi, M., Miyauchi, T., 2004. Effect of turbulence characteristics on local flame structure of H_2-air premixed flames. J. Turbul. 5, 16.

Panchapakesan, N.R., Lumley, J.L., 1993. Turbulence measurements in axisymmetric jets of air and helium. Part 1. Air jet. J. Fluid Mech. 246, 197–223.

Prasad, A.K., 2000. Stereoscopic particle image velocimetry. Exp. Fluids 29, 103–116.

Prasad, A.K., Jensen, K., 1995. Scheimpflug stereocamera for particle image velocimetry in liquid flows. Appl. Opt. 34, 7092–7099.

Scarano, F., Poelma, C., Westerweel, J., 2007, Towards four-dimensional particle image velocimetry. In: Proceedings of the 7th International Symposium on PIV.

She, Z.S., Jackson, E., Orszag, S.A., 1990. Intermittent vortex structures in homogeneous isotropic turbulence. Nature 344, 226–228.

Soloff, S.M., Adrian, R.J., Liu, Z.-C., 1997. Distortion compensation for generalized stereoscopic particle image velocimetry. Meas. Sci. Technol. 8, 1441–1454.

Tanahashi, M., Fukuchi, Y., Choi, G.-M., Fukuzato, K., Miyauchi, T., 2004b, The time-resolved stereoscopic digital particle image velocimetry up to 26.7 kHz. In: Proceedings of the 12th International Symposium on Applications of Laser Techniques and Fluid Mechanics.

Tanahashi, M., Miyauchi, T., Ikeda, J., 1997. Identification of coherent fine scale structure in turbulence. In: IUTAM Symposium on Simulation and Identification of Organized Structures in Flows, pp. 131–140.

Tanahashi, M., Iwase, S., Uddin, Md.A., Miyauchi, T., 1999. Three-dimensional features of coherent fine scale eddies in turbulence. In: Proceedings 1st International Symposium on Turbulence and Shear Flow Phenomena. Begell House Inc., pp. 79–84.

Tanahashi, M., Fujimura, M., Miyauchi, T., 2000. Coherent fine-scale eddies in turbulent premixed flames. Proc. Combust. Inst. 28, 529–535.

Tanahashi, M., Iwase, S., Miyauchi, T., 2001. Appearance and alignment with strain rate of coherent fine scale eddies in turbulent mixing layer. J. Turbul. 2, 6.

Tanahashi, M., Ootsu, M., Fukushima, M., Miyauchi, T., 2002. Measurement of coherent fine scale eddies in turbulent mixing layer by DPIV. Eng. Turbul. Model. Meas. 5, 525.

Tanahashi, M., Fukuchi, Y., Choi, G.-M., Fukuzato, K., Miyauchi, T., 2003. High spatial resolution time-series PIV for turbulence measurement. In: Proceedings of 4th International Symposium on Turbulence, Heat and Mass Transfer, pp. 245–252.

Tanahashi, M., Kang, S.-J., Miyamoto, T., Shiokawa, S., Miyauchi, T., 2004a. Scaling law of fine scale eddies in turbulent channel flows up to $Re_\tau = 800$. Int. J. Heat Fluid Flow 25, 331–340.

Tanahashi, M., Fujibayashi, K, Miyauchi, T., 2007. Fine scale eddy cluster and energy cascade in homogeneous isotropic turbulence. In: IUTAM Bookseries 4 (IUTAM Symposium on Computational Physics and New Perspectives in Turbulence), pp. 67–72.

Upatnieks, A., Driscoll, J.F., Ceccio, S.L., 2002. Cinema particle imaging velocimetry time history of the propagation velocity of the base of a lifted turbulent jet flame. Proc. Combust. Inst. 29, 1897–1903.

van Doorne C.W.H., Hof, B., Lindken, R.H., Westerweel, J., Dierksheide, U., 2003. Time resolved stereoscopic PIV in pipe flow. Visualizing 3D flow structures. In: Proceedings of the 5th International Symposium on PIV.

Vogel, A., Lauterborn, W., 1988. Time resolved particle image velocimetry. Opt. Laser Eng. 9, 277–294.

Wang, Y., Tanahashi, M., Miyauchi, T., 2007. Coherent fine scale eddies in turbulence transition of spatially-developing mixing layer. Int. J. Heat Fluid Flow 28, 1280–1290.

Willert, C., 1997. Stereoscopic digital particle image velocimetry for application in wind tunnel flows. Meas. Sci. Technol. 8, 1465–1479.

Wygnanski, I., Fiedler, H., 1969. Some measurements in the self-preserving jet. J. Fluid Mech. 38, 577–612.